The episodic rise of Salinas de Oro diapir and kinematics of radial faults using paleoseismological techniques (NE Spain). Salt upwelling versus karstic subsidence.

Jesús Guerrero (1)*, Gloria Desir (1), Carles Roqué (2), Mario Zarroca (3), Ivan Fabregat (1).

(1) Departamento de Ciencias de la Tierra; Universidad de Zaragoza; C/. Pedro Cerbuna 12; 50009 Zaragoza; Spain

(2) Àrea de Geodinàmica Externa i Geomorfologia; Universitat de Girona; Campus Montilivi; E-17003 Girona; Spain

(3) Departamento de Geología; Universidad Autónoma de Barcelona; E-08193 Barcelona; Spain

*Corresponding author e-mail: jgiturbe@unizar.es

Abstract

This paper successfully explores the use of trenching and paleoseismological techniques to determine salt flow rates into a salt diapir for the first time in the literature. The Salinas de Oro diapir, located in the northern Spanish Pyrenees, is an oval-shape and steep sides, Triassic-salt dome that extends vertically for more than 7 km down to the Paleozoic basement. Salt dissolution subsidence and diapir growth are ~~coetaneous~~ active processes. Karstification is responsible for the development of large bending and collapse sinkholes, a thick caprock and the monocline folding and ring faulting of the Cretaceous and Early Tertiary limestone rim. The evaporite karstic aquifer discharges high-concentration water of up to 137 g/l of total dissolved solids and a conductivity over 200 mS/cm into the Salado Creek, which drains the diapir top. The salinity

monitoring of this drainage provides a karstic surface lowering rate of around 3.8 mm/year. Salt upwelling has caused the 150 m uplift of the annular limestone escarpment and the development of more than 3000 m long radial grabens with up to 90 m of vertical offset that disrupt drainages, displace quaternary deposits and overprint concentric faults. The 260 cm drag folding of lacustrine facies exposed in a 42 m long and 6.5 m deep trench due to the creep motion of the western radial fault in Azanza Graben yielded a minimum short-term uplift slip rate of 1.78 mm/yr for the last 1461 years and provides a minimum salt supply rate of over 5 mm/yr considering karstification lowering. This value that is more than 800 times higher than average, evidence the discontinuous growth of Salinas de Oro Diapir.

Keywords

Concentric fault, trenching, uplift rate, salt dissolution.

Introduction

The factors that control salt movement in diapirs are crucial variables in order to assess the suitability of a diapir as a repository of waste disposal (Koyi, 2001), the timing of migration and entrapment of potential hydrocarbons in the overburden (Smith et al., 1993; Guglielmo et al., 1999; Stewart and Clarke, 1999), the potential seismic hazard (Lehné and Sirocko; 2010; Choi et al., 2011; Dahm et al., 2011; Wetzler et al., 2011), the impact in regional tectonics (Dooley et al., 2009; Santolaria et al., 2015) and the effects on the topography, hydrology and geomorphology of salt regions (Holford et al., 2007; Bruthans et al., 2010; Guerrero et al., 2015).

According to Koyi (2001) the rising rate of salt structures mainly depends on the effective viscosity of salt, differential loading of the overburden units, the dimension of

the feeding stem, the thickness of the feeding salt layer, the maturity of salt structures and the regional tectonic stress. Depending on these factors the mean uplift rates of salt diapirs varies between 0.01 to 15 mm/yr (Koyi, 2001; Bruthans et al., 2006). Several methodologies have been used to report long-term and present-day uplift rates of emergent salt diapirs. Many authors have reported uplift rates ~~of salt diapirs~~ in different areas based on the displacement of deformed strata and sediments on top of the crest of the diapiric structure such as Jackson and Seni (1983) in several salt domes in Texas (0.45 mm/yr), Davison et al. (1996) in Yemen (4.5 mm/yr; Jabal AI Milh diapir), Zirngast (1996) in the northern Germany (0.1–0.5 mm/yr; Gorbelen salt dome), Autin (2002) in Lousiana (2 mm/yr; Five Islands domes), Bruthans et al. (2006) in Iran (1-5 mm/yr; Hormoz and Namakdan diapirs) and Frumkin (1996) in Israel (6-7 mm/yr; Mount Sedom diapir). Recently, ~~the~~ investigations dealing with salt structures have experienced a substantial momentum, largely due to the precise measurement of the ground displacement by ~~G~~ground ~~S~~urvey ~~T~~echniques and ~~R~~emote Sensing ~~M~~ethods that complement conventional geological data. For instance, these techniques have been successfully applied in the salt-related fault system of the Gulf of Mexico integrating data from GPS, Synthetic Aperture Radar Interferometry (InSAR) and LIDAR and (Huang, 2012; Han, 2013; Yu and Wang, 2016), the Mount Sedom diapir by precise leveling and InSAR (Weinberger, 2006; Frumkin, 2009) and the Axel Heiberg Island diapirs in the Canadian High Arctic using Polarimetric SAR Interferometry (PolInSAR) (Harrington, 2018). In Spain, despite salt diapirs are common geological structures in the Pyrenees (e.g., Serrano and Martínez del Olmo et al., 1990 and 2004; Sans and Verges, 1995; Pinto et al., 2005; Ferrer et al., 2012; Quinta et al., 2012; Poprawski et al., 2014) and Betics (e.g., De Ruig, 1995; Calaforra and Pulido-Bosch, 1999) most of the works deal with the penetration mechanisms, fracture pattern and basin stratigraphic

architecture to study potential hydrocarbon reservoirs and ignore their past and current moving rates. Only Sans (2003) in the Cardona Diapir, Lucha et al. (2008) in the Barbastro salt-cored anticline, Gracia et al. (2008) in the Strait of Gibraltar and Poprawski et al. (2014) measured diapir rising rates of around 1, 0.3, 0.6 and up to 6.8 mm/yr, respectively, using geodetic measurements or displaced terraces and sediments as markers.

This paper explores the suitability of combining trenching, classical geologic mapping and hydrological studies for detailed diapir characterization. Despite trenching is mainly utilized in seismic hazard assessments (McCalpin, 2009), a large number of research manuscripts evidence the successful use of this technique to study gravitational deformation processes such sinkholes (Gutiérrez et al., 2011, Carbonel, 2014), gravitational faults related to interstratal karstification of salt (Gutiérrez et al., 2012, 2014, Guerrero et al., 2015), sackungs (Gutiérrez et al., 2005; 2008) and landslides (McCalpin y Hart, 2003). The approach was tested in the Salinas de Oro piercing diapir, in the northwestern Pyrenees in Spain, a relatively wet region (1200 mm/yr of rainfall) where salt is outcropping and consequently, dissolving fast (Fig. 1). Karstic subsidence and diapir growing rates will be compared in order to determine the dominant process that controls the structural configuration of the diapir. To our knowledge, this is the first paper in the international literature that addresses a detailed characterization of a diapiric structure and displacement rates using paleoseismological techniques.

Geological setting

The Salinas de Oro salt diapir is a classic oval-shape Lower Cretaceous diapir with an area of 18.4 km^2, very steep sides and no overhangs that extends vertically for more

than 7 km down to Paleozoic basement (IGME, 1990a, b; Pinto et al. 2005). It consists of Keuper and Muschelkalk halite interlayered with anhydrite, gypsum, shale, limestone and dolomite and intruded mafic volcanic rocks (Olive et al., 2010). Although halokinetic processes started during the opening of the North Atlantic in Lower Cretaceous under an extensional tectonic regime (Salvany, 1990; García-Mondéjar, 1996; Serrano and Martinez del Olmo, 2004), the Salinas de Oro diapir didn't pierce the surface until the end of the Cretaceous due to the convergence of the Iberian and European plates (Muñoz, 1992). After this period of tectonic shortening and salt uplift, a stage of thermal subsidence occurred and the area underwent a succession of transgressions and regressions from the Maastrichtiense to the Eocene. This led to a thick sequence of calcarenites and bioclastic limestones that covered the salt diapir (Castiella et al., 1982; Ramírez et al., 1987; Salvany, 1990). The strata deposited during this period are from base to top (Olive et al., 2010) (Fig.1): (1) 50 m of Upper Cretaceous marls; (2) up to 250 m thick Paleocene dolomites, bioclastic limestones and marls; (3) 130 m thick of Lower Eocene calcarenites and limestones; (4) 350 m thick of Middle Eocene cross-bedded limestones and bioclastic calcarenites and (5) 600 m thick Middle and Upper Eocene grey marls of 40 to 37 Ma according to their planktonic foraminifera assemblage (Payros et al., 1996; Payros, 1997). A reactivation of Salinas de Oro diapir occurred from the beginning of the Oligocene to Middle Miocene in relation with the development of the Ebro Foreland Basin, and the accumulation of several thousand of meters of endorheic continental sediments related to thrust loading (Vergés et al., 2002). During this halokinetic period, the Mesozoic and Early Tertiary carbonate sequence were pierced and uplifted more than 150 m above their surroundings to form an annular limestone escarpment with vertical beds at the contact with the Triassic evaporites progressively decreasing their dips outwards from the

125 diapir. Since the Middle Miocene, a change in the tectonic regime from compressional
126 to extensional allowed the top of the salt diapir to undergo intense erosion and karstic
127 dissolution.
128
129
130 **Methodology**
131 The geological and geomorphological maps of Salinas de Oro diapir produced by Olive
132 et al. (2010) and Guerrero (2017) constituted highly useful documents for the bedrock
133 geology, distribution of radial and concentric fault scarps and faulted Quaternary
134 deposits. The Azanza Graben was selected for the trenching investigation in order to
135 determine growing diapir rates due to its easy access for the backhoe and the existence
136 of a lacustrine area that increases the possibility of finding a fine-grained stratigraphic
137 sequence and radiocarbon datable material. The geological map of Azanza Graben was
138 refined in the field using color 1:5,000 scale orthophotographs to better locate the trench
139 that was oriented perpendicularly to the strike of the eastern radial fault. We followed
140 the procedure for logging paleoseismological trenches as described by McCalpin
141 (2009). The charcoal collected from the excavated deposits were dated at DirectAMS
142 radiocarbon dating services in Seattle using Accelerated Mass Spectrometry, and the
143 ages were calibrated using the CALIB 7.1 software (Stuiver et al., 2019).

144 In order to characterize salt dissolution rates and the main hydrochemical features of the
145 evaporitic aquifer, two sampling stations (stations A and B) together with 4 brine
146 springs were included in this study (Fig. 1, Table 1). Two sampling surveys were
147 carried out in May 2017 and September 2018 and included the major ion
148 concentrations, electrical conductivity (EC), temperature (T) and total dissolved solids
149 (TDS). The samples were analyzed in the Hydrochemistry Laboratory of the

Department of Earth Sciences of the University of Zaragoza, Spain. Alkalinity and chloride contents were determined by titration with a Mettler titrator with end-point electrode and sulfate concentrations by colorimetry. Inductively Coupled Plasma-Atomic Emission Spectrometry (ICP-AES) was used for the analyses of cations (Ca, Mg, Na and K). Geochemical calculations were performed with the PHREEQC code (Parkhurst and Appelo, 2013) using the pitzer.dat database. The calculated charge balance error for the reported samples, as calculated with the PHREEQC code, is always below 5%. The hydrochemical information of Estenoz gauging station (Table 2) was obtained from the public database of the Ebro Waters Authority (Confederación Hidrográfica del Ebro; CHE).

The geomorphology of the diapir crest

The present topography and structural configuration of Salinas de Oro diapir comes up from the balance between passive diapirism and karstification. A detailed description of the structural configuration of the diapir can be found in Guerrero (2017). Diapirism has uplifted the Mesozoic and Tertiary Limestone sequence more than 150 m to form an annular limestone escarpment with dips of 75º at the contact with the Triassic evaporites that progressively decrease to 20º outward from the diapir. In addition, the limestone overburden was breached into more than 3000 m long radial grabens with up to 90 m of vertical offset (Figs. 1, 2A, 2B).

The most significant karstic evidences are the occurrence of sinkholes at the bottom of the valley and a ring-faulting structure at the edges of the diapir (Fig. 1). At the diapir center, the dissolution of salt has transformed the diapir top into a 300 m deep topographic depression covered by a thick caprock of more than 100 m in outcrop composed of distorted clays with thick bodies of mafic rocks. The caprock is affected

by a large number of rounded to irregular shape, bending and collapse sinkholes up to 310 m in diameter and 70 m deep (Fig. 2D). At the flanks of the diapir, a ring monocline with limb-dips between 10 and 45º is broken by a swarm of synthetic and antithetic inward-dipping normal annular faults that offset the limestone escarpment (Figs 2B, 2D). This chaotic structure creates a outstanding landscape characterized by a stepped sequence of circular ridges and grabens bounded by uphill-facing scarps and linear ground hollows up to 50 m long and 4 m wide that disrupt the drainage system creating defeated streams on the hanging wall and beheaded drainage channels in the footwall. In addition, large collapse sinkholes of 20 to 150 m in diameter occur primarily at the intersection between radial and concentric faults. The bigger and deeper sinkholes may intercept the limestone aquifer water table and become permanent lakes with a low conductivity of around 0,65 mS/cm and an oscillating surface water level depending on the rainfall rate. The development of sinkholes and a ring-faulting arrangement in the limestone rim is related to the continuous interstratal karstification of the salt at the contact with the carbonate overburden that causes the passive bending and gradual unfolding, tilting and final faulting of the overlying cover towards the center of the diapir and the collapse of large salt-dissolution cavities (Guerrero, 2017).

The cross-cutting fracture pattern related to the interaction between karstic subsidence and salt doming processes is dominated by the truncation of concentric faults by radial grabens. Radial faults overprint the monocline and ring faults that may be offset several tens of meters and become covered by slope deposits along main radial grabens bottom (Fig.1, 2B). This overprinting configuration together with the disruption of the drainage network, the displacement of stream and colluvial deposits and the development of

sinkholes and linear troughs along radial faults suggest that diapirism is still an active process (Guerrero, 2017).

Hydrogeology of the diapir

The area is characterized by two interconnected and unconfined karstic aquifers: i) the evaporitic aquifer developed in the thick caprock on top of the salt diapir and ii) the fractured and highly permeable limestone escarpment aquifer ~~at~~ the flanks of the diapir that collect most of the rainfall and discharges fresh water into the previous one. The Salado Creek that dissects through 100 m thick caprock in a North-South direction and drains the top of the diapir and the tertiary limestone escarpment, acts as the base level for both aquifer systems.

The spatial distribution of sinkholes is clearly conditioning the hydrogeology of both aquifers. Runoff along the diapir flanks quickly infiltrates through large intrastratal collapse sinkholes disrupting runoff, feeding the limestone aquifer and ultimately recharging the underlying evaporitic endokarst system. The entrance of freshwater favors the interstratal dissolution of salt and consequently, the enlargement of sinkholes and the passive bending and faulting of the limestone annular sequence in a feedback-process. Five high-concentration perennial springs (S1 to S5) discharge into the Salado Creek along the bottom of the valley with TDS up to 137 g/l and pH values increasing with salinity between 7.01 to 7.84 (Figs. 1, 2E, 2F, Table 1). All the water samples are slightly saturated with respect to calcite and dolomite, close to saturation with respect to gypsum and anhydrite and still far from the equilibrium with respect to halite despite their high salinity, as determined by PHREEQC model (Parkhurst and Appelo, 2013). These saturation indexes are consistent with the dissolution of carbonates in the diapir

flanks that explains calcite and dolomite saturation and the predominance of gypsum and anhydrite in the caprock that causes sulfate saturation. The relations between the molar dissolved contents of Na/Cl and Ca/SO_4 show a good 1:1 correlation (Fig. 3). This analytical result can be attributed to halite and gypsum/anhydrite dissolution respectively, as the main source for Na, Cl, Ca and SO_4 in the hydrogeological system, which is in agreement with the mineralogy of the evaporitic bedrock. Despite this strong hydrochemical parameters correlations, the S1 spring waters show a different evolution trend with constant Ca values at increasing sulfate and magnesium concentrations. This pattern probably matches a dedolomitization process responsible for the dissolution of dolomite and the precipitation of calcite in the presence of calcium sulfate rich flowing fluids (Evamy, 1967; Wierzbicki et al., 2006; Hallenberger et al., 2018) according to this reaction (Larsen and Chilingar, 1983):

$$CaMg(CO_3)_2 + CaSO_4 \leftrightarrow 2CaCO_3 + Mg^{2+} + SO_4^{2-}$$

This two evolution trends demonstrate that flow paths of S1 saline waters might completely differ from S2 to S5 brine waters ones and that S1 brines probably cross through Triassic dolomite beds interbedded in the Keuper facies in order to explain dedolomitization.

The salinity, conductivity and chemistry values of the Salado Creek at stations A and B (See location in Fig.1) before the discharge of brines S1 to S4 and at the southern diapir edge, respectively, are shown in table 1. These hypersaline waters cause a dramatic increase in the salinity of the Salado Creek from around 4 mS/cm to more than 85 mS/cm despite most of the S2 and S3 salty water is diverted to feed more than 300 solar evaporation salterns to exploit the salt for industrial uses. TDS (Total Dissolved Solids) also increases from less than 4 g/l to 61 g/l during the wet season and 70 g/l during the

dry season between the two stations. According to Ebro Waters Authority (Confederación Hidrográfica del Ebro, CHE) the measured average annual discharge of the Salado Creek in a gauging station located 2 km South of Salinas de Oro Diapir is around $3{,}53 \cdot 10^6$ m^3/yr. The minimum, maximum and average water conductivity and TDS at this point were 24.1, 104.5 and 52.3 mS/cm and 16.9, 84.9 and 43.8 g/l, for a monitoring period of 7 years between 2007 and 2013 (Table 2).

Considering the mean TDS and annual discharge of ~~the~~ Salado Creek ~~mentioned before~~, we can approximately estimate around $150 \cdot 10^3$ metric tons of dissolved halite and gypsum per year. This is equivalent to the creation of a void with a volume of around $70*10^3$ m^3 per year, assuming a specific gravity of 2.23 g/cm^3 for the dissolved salts. This rough value implies a karstic surface lowering rate of around 3.8 mm/year during the monitoring period assuming a total diapir area of 18.4 km^2.

Diapir growing rate

The Azanza Graben is a 1.14 km^2 radial graben with conspicuous geomorphic expression and located in the north flank of the diapir, is the result of the extension of the limestone overburden during diapir uplift (Figs. 1, 2C, 4). The graben is delimited by two prominent normal radial faults of 4200 m long and 1.5 times the radius of the salt diapir, a value that is in agreement with the ones obtained in analog models (Alsop, 1996; Yamada et al., 2005; Stewart, 2006). The faults cut across the tilted Mesozoic and Tertiary limestone sequence whose beds rapidly decrease their N-dip away from the diapir from 20º to 5º. These rupture surfaces overprint the ring monocline and annular faults associated to karstic subsidence pointing to its activity (Figs. 1, 4). Mapping reveals that strata gradually dip toward the fault scarps due to dragging to form a

normal-faulted drag monocline in the hanging wall with forelimb dips of around 30º (Fig. 4). Therefore, these fault scarps results from the throw on the radial fault and the forced folding associated with the drag fold. The height of the fault scarps that is representative of the minimum vertical displacement of the overburden decreases progressively from 65 m and 90 m in the western and eastern flanks respectively, to meter-throw faults with increasing distance from the diapir center. These values that yields an estimated displacement to length ratio (Dmax/L) of 0.02 and 0.027 for the eastern and western faults respectively, are comparable with those reported for gravitational faults (Gutiérrez et al., 2012, 2014; Carbonel et al., 2013; Guerrero et al., 2015).

The karstification processes of the limestone rim are intense along the trace of the radial fault leading to several sinkholes (Figs. 2C and 4). The bigger ones that are flooded all year round are more than 50 m in diameter since they intercept the shallow water table of the limestone aquifer. This aquifer discharges into a fresh water spring that supplies drinking water to Azanza village and is the source of a little creek at the center of the graben. The movement of the radial faults is disrupting the drainage network. The creek that drains Azanza Graben is blocked by the movement of the western radial fault creating a closed depression with a temporal lake and lacustrine sedimentation in the downthrown block. At the southern margin, subsidence of Azanza graben has breached the annular limestone escarpment and consequently, a stream reach that used to drain several concentric depressions and flowed southward towards the diapir center, was abandoned and now discharges northward into Azanza graben (Fig. 4).

A 42 m long and 6.5 m deep trench was dug into the hanging wall of the western radial normal fault perpendicular to its trace and 4200 m away from the diapir center where

the height of scarp was less than 4 m (Fig. 5). The trench exposed a relatively simple structure constituted by slightly dipping fine-grained sediments unconformably lying on an alternating limestone and marl, weathered and fractured sequence of Eocene age. The graben fill is made up of three units that are from base to top: (1) a 0.5 m thick, grey to light brown lacustrine massive clay with ferruginous and carbonate nodules; (2) 1.4 m thick, bioturbated fine-grained silty slope deposits unconformably overlying the lacustrine sediments; (3) a 0.4 m thick soil on top. Two samples collected at the base of the lacustrine and slope sediments yielded calibrated radiocarbon ages of 1361±55 yr BP (1461-1306) and 1217±45 yr BP (1262-1172). The bedrock strata mainly accommodates throw by bending and undergo an abrupt change in dip from 10º to 35º E to form a monocline (Fig. 5). Most of the fractures did not displace bedrock except for faults F1, F2 and F3 that account for a cumulative vertical displacement of just 30 cm. These fractures are truncated by the overlying graben fill what evidence their inactivity in the last millennium and support the passive bending deformation style of the substratum and graben fill associated to salt rising. Using the base of the lacustrine sediments as a marker, and assuming a horizontal original attitude, we can estimate a vertical displacement of 260 cm due to folding and a mean long-term deformation rate of 1.78 mm/yr for a time span of 1461 years. This datum has to be considered a minimum value since tilted lacustrine sediments have been partly eroded by the overlying unit and haven´t been completely exposed in the trench. Given that throw of the radial fault attenuates towards its tip, it is expected that the rate of salt rising and radial fault slip were much higher than the obtained in the trench.

Discussion

Guerrero (2017) using the age of the top of the limestone sequence as a geologic marker estimated a net vertical displacement of the overburden rim related to karstic sagging and collapse of around 90 m and an average subsidence rate of 0.002 mm/yr over the past 37 Ma in the Salinas de Oro Diapir. However, the large number of sinkholes at the diapir roof, the existence of open fissures in the hanging-wall of concentric faults and the disruption of the drainage network point to a subsidence ratio higher than average. Runoff and spring water salinity measurements corroborates that salt karstification is currently a very active process. Water mass balance of the Salado Creek yielded a rough dissolution lowering rate of the diapir roof of around 3.8 mm/yr for a monitoring period of 7 years, a datum that is 1900 higher than average and points to a discontinuous dissolution. Several recent trenching investigations demonstrate that salt-dissolution induced-faults show an episodic displacement style (e.g., Gutiérrez et al., 2012, 2014; Carbonel et al., 2013). Any change in the base level, precipitation rate, temperature, pressure, chemistry and velocity of underground flows, area affected by dissolution or mechanical strength of the overburden result in increases or reductions in the dissolution rate of evaporites and contributes to the episodic behavior of karst (Guerrero, 2017). In addition to all this variables, the alternating sequence of quiescence and growing stages seems to favor changes in the intensity of karstification in salt domes. The warping and breaching of the overburden usually end exposing the salt at the diapir top. This leads to intense evaporite dissolution, the formation of large voids, sinkholes and maze caves (e.g., Frumkin, 1996, 2009; Lucha et al., 2008) and consequently the subsidence accommodation of the overburden strata on top of the diapir roof by a combination of sagging and annular faulting (Gutiérrez, 2004; Carbonel et al., 2013; Guerrero et al., 2015). This sinking phenomenon that has already been described in other analog ~~geologic~~ landforms like pingos (Mackay, 1998; Burr et al.,

2006) and calderas (Walter and Troll, 2001; Holohan et al., 2005), is often coeval to salt rising. The Mount Sedom in Israel (Frumkin, 1996, 2009), Gulf Coast salt domes in Texas (Huang, 2012) and salt diapirs in Iran (Bruthans et al., 2006, 2010) are some examples of the coexistence of these two geological mechanisms. Once salt flow into the diapir is abruptly reduced or stopped and the diapir entries into a quiescence period, the development of a thick insoluble dissolution residue on top of the diapir might partly inhibit karstification in a similar way as clay sediments settling at the bottom of salt caves impede further vertical dissolution (Frumkin, 1996). The hydrogeological studies of Iranian salt domes support that the occurrence of a karstic residue cap exerts a critical drop in the surface dissolution rate (Bruthans et al., 2017; Zarei and Raeisi, 2010; Zarei, 2016). Here, water concentrations measured in runoff partly derived from salt exposures were halite-rich and had high to very high TDS values between 50 g/l to more than 330 g/l, while the dissolved halite content of runoff from even very thin cap soils of less than 2 m was very low and sometimes did not exceed 0.5 g/l, exponentially decreasing with time.

Using geologic markers, the minimum average vertical growth of the Salinas de Oro diapir was estimated to be around 0.004 mm/yr considering 150 m uplift of the limestone rim (Guerrero, 2017). However, the 260 cm offset of lacustrine sediments in Azanza Graben, 4200 m away from the diapir center and close to the tip of the fault evidenced a minimum salt rising rate of 1.78 mm/yr due to bending for the last 1461 years. Despite this upwelling ratio is 400 times higher than average, it is expected to significantly increase and exceed subsidence at the diapir flanks at the contact between the salt dome and limestone overburden where fault scarp reaches up to 90 m high (20 times higher than at the tip). Bruthan et al. (2006) detailed studies in Hormoz and

373 Namakdan diapirs demonstrated that the gradual increase in the uplift rate of circular
374 diapirs from the margins towards the diapir center fits a parabolic profile of Newtonian
375 fluid and so, the rise rate in the center is often over 2-6 times higher than at the margin
376 depending on salt flow velocity. Assuming these numerical relationships and
377 considering that the trench in Azanza graben was dug at its end, the growing rate of
378 Salinas de Oro diapir might reach up to 8 mm/yr.
379
380 The difference between the long-term and short-term upwelling ratios in Salinas de Oro
381 Diapir supports the episodic behavior of the rising phenomenon in agreement with the
382 history of most salt domes that includes long periods of quiescence interrupted by
383 growing pulses (Vendeville and Nilsen, 1995; Harding and Huuse, 2015). Nevertheless,
384 the kinematic of radial faults determined from the structural arrangement of the
385 sedimentary fill and bedrock in Azanza Graben apparently disagrees with the episodic
386 movement of the Salinas de Oro Diapir. The lack of fissure fills, colluvial wedges and
387 large unconformities that might record sudden surface ruptures (McCalpin, 2009)
388 together with the inactivity of faults F1 to F3 in the last 1461 years and the progressive
389 bending of the lacustrine deposits and Eocene bedrock fit better with the creep motion
390 rather than the episodic slip of the radial faults. This apparent controversy suggests that
391 although diapir growth is discontinuous in the long-term (quiescence stages and pulses),
392 there seems to be a continuous supply of salt during the growing periods that explains
393 the creeping behavior of radial faults. On the other hand, although diapir growing
394 periods are often correlated with regional tectonics (Vendeville and Jackson, 1992;
395 Hudec and Jackson, 2007), geodetic measurements of extensional deformation across
396 the 150 km wide Pyrenees of around 0.5 and 0.2 mm/yr (Asensio et al., 2012; Nocquet,
397 2012) are between 3 to 8 times lower than the minimum slip rate of Azanza Graben and

doesn´t support the exclusive tectonic genesis for the current episodic growth of Salinas de Oro Diapir. Probably, the differential loading related to a North dipping basement fault and 1500 m thick difference in sediment thickness between the feeding area and the Salado Creek Valley may be responsible in part for the lateral flow of salt into the Salinas de Oro diapir (Guerrero, 2017).

The prevalence of either subsidence or salt upwelling would determine the cross-cutting relationships between ring and radial faults and consequently the structural configuration of the diapir roof. In the Salinas de Oro diapir, the radial breaching of the limestone rim, the development of fault scarps that disrupt drainage and the overprinting of radial grabens on ring subsidence-induced faults evidence that the rising-subsidence ratio is notably higher than 1. According to the geological markers, the average uplift rate of the limestone overburden is double than subsidence. In the present time, considering the slip rate of Azanza Graben and Bruthans et al. (2006) numerical relationships, the current uplift rate of Salinas de Oro diapir would be up to 8 mm/yr, which would double again the present subsidence rate. These data suggest that dissolution subsidence might roughly be around half diapir uplift and consequently is partly compensating salt flow. Since there is no evidence of salt extrusion, the rate of salt supply would be approximately equal to the sum of karstification and diapir roof uplift rates (Hudec and Jackson, 2007; Poprawski et al., 2014). As a result, salt flow velocity would be around 0.006 mm/yr in the long-term and between 5 and 12 mm/yr in the present considering the minimum or maximum slip ratio of Azanza Graben, respectively. This last value which is more than 800-2000 times higher than average places the Salinas de Oro Diapir as the fastest quaternary growing diapir of the Spanish territory in the published literature so far (e.g.; Sans, 2003, Lucha et al., 2008; Gracia et

al., 2008). On the other hand, the more marked geomorphic expression of the radial grabens located on the east, west and north flanks points to an asymmetric uplift and probably indicates that upward salt emplacement is not accomplished as a single uniform mass of rock salt but by the movement of individual salt spines with different rates of vertical movements. Unfortunately, the trenching study of Azanza Graben does not allow an accurate estimation of diapir growth velocity in the entire salt top and consequently the measured uplift rate has to be carefully taken. Extended trenching surveys and precise uplift monitoring using ground survey techniques and remote sensing methods used successfully in other salt domes (e.g., Weinberger, 2006; Looff et al., 2010; Huang, 2012; Han, 2013; Yu and Wang, 2016), will provide further information to infer the asymmetry and diachrony of salt flow and precise uplift-subsidence ratios in the Salinas de Oro Diapir.

Conclusions

In continental settings, salt diapirism and dissolution subsidence are often coetaneous and their relative activity would influence the geomorphic expression of the diapir top. In the Salinas de Oro diapir, radial grabens cut across ring faults, disrupt drainage and displace Quaternary deposits evidencing active salt-flow and diapir rise. This structural configuration is supported by an average growing-subsidence ratio over 1. The 260 cm tilting of the lacustrine sediments exposed in the Azanza Graben trench yield a growing rate of the diapir of 1.78 mm/yr for the last 1,461 years. This value has to be considered a minimum since the trench was done close to the tip of the radial fault and it is expected to exceed karstification rate that was estimated to be around 3.8 mm/yr for a monitoring period of 7 years from runoff water mass balance.

The notably difference between the long-term and short-term diapir growing rates evidences a currently active rising period and an episodic diapirism. Despite the discontinuous rising of the Salinas de Oro Diapir in the long term, the lack of surface ruptures signs and the flexural accommodation of the overburden in response to the creeping motion of radial faults suggest that there is a continuous supply of salt into the diapir during pulses.

The estimation of diapir roof uplift by accurate paleoseismological techniques is a precise and novel approach to constrain rates of halokinesis in salt diapirs, compare changing growing rates over time and determine the kinematics of radial faults.

Acknowledgments

The research has been funded by the Spanish national project CGL2017-85045-P (Ministerio de Economia, Industria y Competitividad) and the Young Researchers project 221-409 (University of Zaragoza).

References

Alsop, G.I., 1996. Physical modeling of fold and fracture geometries associated with salt diapirism. In: Alsop, G.I., Blundell, D.J., Davison, I. (Eds.), Salt Tectonics. Geological Society, London, Special Publication 100, pp. 227–241.

Asensio, E., Khazaraddze, G., Echeverria, A., King, R.W., Vilajosana, I., 2012. GPS studies of active deformation in the Pyrenees. Geophysical Journal International 190, 913–921.

469 Autin, W.J., 2002. Landscape evolution of the Five Islands of south Louisiana:
470 scientific policy and salt dome utilization and management. Geomorphology 47, 227–
471 244.

472 Bruthans, J., Filippi, M., Geršl, M., Zare, M., Melková, J., Pazdur, A., Bosák, P., 2006.
473 Holocene marine terraces on two salt diapirs in Persian Gulf (Iran): age, depositional
474 history and uplift rates. Journal of Quaternary Science 21, 843–857.

475 Bruthans, J., Filippi, M., Zare, M., Churáčková, Z., Asadi, N., Fuchs, M., Adamovič, J.,
476 2010. Evolution of salt diapir and karst morphology during the last glacial cycle: Effects
477 of sea-level oscillation, diapir and regional uplift, and erosion (Persian Gulf, Iran).
478 Geomorphology 121, 291–304.

479 Bruthans, J., Kamas J., Filippi, M., Zare, M., Mayo, A.L., 2017. Hydrogeology of salt
480 karst under different cap soils and climates (Persian Gulf and Zagros Mts., Iran).
481 International Journal of Speleology 46, 303–320.

482 Burr, D.M., Tanaka, K.L., Yoshikawa, K., 2009. Pingos on Earth and Mars. Planetary
483 and Space Science 57, 541–555.

484 Calaforra, J.M., Pulido-Bosch, A., 1999. Gypsum karst features as evidence of diapiric
485 processes in the Betic Cordillera, Southern Spain. Geomorphology 29, 251–264

486 Carbonel, D., Gutiérrez, F., Linares, R., Roqué, C., Zarroca, M., McCalpin, J., Guerrero,
487 J., Rodríguez, V., 2013. Differentiating between gravitational and tectonic faults by
488 means of geomorphological mapping, trenching and geophysical surveys: The case of
489 the Zenzano fault (Iberian Chain, N Spain). Geomorphology 189, 93–108.

490 Carbonel, D., Rodríguez-Tribaldos, V., Gutiérrez, F., Galve, J.P., Guerrero, J., Zaroca,
491 M., Roqué, C., Linares, R., McCalpin, J.P., 2014. Investigating a damaging buried

492 sinkhole cluster in an urban area integrating multiple techniques: geomorphological
493 surveys, DInSAR, GPR, ERT, and trenching. Geomorphology 229, 3–16.

494 Castiella, J., Sole, J., Segismundo, N., Otamendi, A., 1982. Las Aguas subterráneas en
495 Navarra. Proyecto hidrogeológico, Diputación Foral de Navarra, Industrias Gráficas
496 Castuera, Burlada, 229 pp.

497 Choi, S., Götze, H.J., Meyer, U., Desire Group, 2011. 3D density modeling of
498 underground structures and spatial distribution of salt diapirism in the Dead Sea Basin.
499 Geophysical Journal International 184, 1131–1146.

500 Dahm, T., Heimann, S., Bialowons, W., 2011. A seismological study of shallow weak
501 micro-earthquakes in the Urban area of Hamburg city, Germany, and its possible
502 relation to salt dissolution. Natural Hazards 58, 1111–1134.

503 Davison I, Bosence D, Alsop GI, Al-Aawah H. 1996. Deformation and sedimentation
504 around active Miocene salt diapirs on the Tihama Plain, northwest Yemen. In: Alsop,
505 G.I., Blundell, D.J., Davidson, I. (Eds.), Salt Tectonics. Geological Society, London,
506 Special Publication 100, pp. 23–39.

507 De Ruig, M.J., 1995. Extensional diapirism in the Eastern Prebetic foldbelt,
508 Southeastern Spain. In: Jackson, M., Roberts, D., Snelson, S. (Eds.), Salt Tectonics: a
509 Global Perspective. AAPG Memoir 65, Tulsa, Oklahoma, pp. 353–367.

510 Dooley, T.P., Jackson, M.P.A., Hudec, M.R., 2009. Inflation and deflation of deeply
511 buried salt stocks during lateral shortening. Journal of Structural Geology 31, 582–600.

512 Evamy, B.D., 1967. Dedolomitization and the development of rhombohedral pores in
513 limestones. Journal of Sedimentary Petrology 37, 1204–1215.

514 Ferrer, O., Jackson, M.P.A., Roca, E., Rubinat, M., 2012. Evolution of salt structures
515 during extension and inversion of the Offshore Parentis Basin (Eastern Bay of Biscay).

In: Alsop, G.I., Archer, S.G., Hartley, A.J., Grant, N.T., Hodgkinson, R. (Eds.), Salt Tectonics, Sediments and Prospectivity. Geological Society, London, Special Publications 363, 361–379.

Frumkin, A., 1996. Uplift rate relative to base-levels of a salt plug (Dead Sea Basin) as indicated by cave levels. In: Alsop, G.I., Blundell, D.J., Davidson, I. (Eds.), Salt Tectonics. Geological Society, London, Special Publication, 100, pp. 41–47.

Frumkin, A., 2009. Formation and dating of a salt pillar in Mount Sedom diapir, Israel. GSA Bulletin 121, 286–293.

García-Mondéjar, J., 1996. Plate reconstruction of the Bay of Biscay. Geology 24, 635–638.

Gracia, F.J., Rodríguez-Vidal, J., Cáceres, L.M., Belluomini, G., Benavente, J., Alonso, C., 2008. Diapiric uplift of an MIS 3 marine deposit in SW Spain: Implications for Late Pleistocene sea level reconstruction and palaeogeography of the Strait of Gibraltar. Quaternary Science Reviews 27, 2219–2231.

Guerrero, J., Brunh, R.L., McCalpin, J., Gutiérrez, F., Willis, G., 2015. Salt-dissolution faults versus tectonic faults from the case study of salt collapse in Spanish Valley, SE Utah (USA). Lithosphere 7, 46–58.

Guerrero, J., 2017. Dissolution collapse of a rising diapir from radial, concentric and salt-withdrawal faults overprinting in Salinas de Oro salt plug, N Spain. Quaternary Research 75, 1–19.

Gutiérrez, F., 2004. Origin of the salt valleys in the Canyonlands section of the Colorado Plateau: Evaporite-dissolution collapse versus tectonic subsidence. Geomorphology 57, 423–435.

539 Gutiérrez, F., Acosta, E., Ríos, S., Guerrero, J., Lucha, P., 2005. Geomorphology and
540 geochronology of sackung features (uphill-facing scarps) in the Central Spanish
541 Pyrenees. Geomorphology 69, 298–314.

542 Gutiérrez, F., Ortuño, M., Lucha, P., Guerrero, J., Acosta, E., Coratza, P., Piacentini, D.,
543 Soldati, M., 2008. Late Quaternary episodic displacement on a sackung scarp in the
544 central Spanish Pyrenees. Secondary paleoseismic evidence?. Geodinámica Acta 21, 4,
545 187–202.

546 Gutiérrez, F., Carbonel, D., Guerrero, J., McCalpin, J.P., Linares, R., Roque, C.,
547 Zarroca, M., 2012. Late Holocene episodic displacement on fault scarps related to
548 interstratal dissolution of evaporites (Teruel Neogene Graben, NE Spain). Journal of
549 Structural Geology 34, 2–19.

550 Gutiérrez, F., Carbonel, D., Kirkham, R.M., Guerrero, J., Lucha, P., Matthews, V.,
551 2014. Can flexural-slip faults related to evaporite dissolution generate hazardous
552 earthquakes? The case of the Grand Hogback monocline of west-central Colorado.
553 Geological Society of America Bulletin 126, 1481–1494.

554 Guglielmo, G., Vendeville, B.C., Jackson, M.P.A., 1999. Isochores and 3D
555 visualizations of rising and falling slat diapirs: Marine and Petroleum Geology16, 849–
556 861.

557 Hallenberger, M., Reuning, L., Schoenherr, J., 2018. Dedolomitization Potential of
558 Fluids from Gypsum-to-Anhydrite Conversion: Mass Balance Constraints from the Late
559 Permian Zechstein-2-Carbonates in NW Germany. Geofluids ID 1784821.

560 Han, X., 2013. Integrated remote sensing and geophysical study of the Hockley Fault in
561 Harris and Montgomery Counties, Texas. MSc Thesis. University of Houston, 72 pp.

562 Harding, R., Huuse, M., 2015. Salt on the move: Multi stage evolution of salt diapirs in
563 the Netherlands North Sea. Marine and Petroleum Geology 61, 39–55.

564 Harrington, E.M., 2018. Polarimetric SAR as a Tool for Remote Sensing Salt Diapirs,
565 Axel Heiberg Island, Nunavut. MSc Thesis. University of Ontario, 120 pp.

566 Holford, S., Thomson, K., Gaffney, V., 2007. Salt tectonics in the Southern North Sea:
567 controls on late Pleistocene-Holocene geomorphology. In: Gaffney, V., Thomson, K.,
568 Fitch, S. (Eds.), Mapping Doggerland: the Mesolithic Landscapes of the Southern North
569 Sea, Archaeopress, Oxford, pp. 61–66.

570 Holohan, E.P., Troll, V.R., Walter, T.R., Münn, S., McDonnell, S., Shipton, Z.K., 2005.
571 Elliptical calderas in active tectonic settings: an experimental approach. Journal of
572 Volcanology and Geothermal Research 144, 119–136.

573 Hudec, M.R., Jackson, M.P.A., 2007. Terra infirma: understanding salt tectonics. Earth
574 Science Reviews 82, 1–28.

575 Huang, Z.Y., 2012. Multidisciplinary investigation of surface deformation above salt
576 dome in Houston, Texas. MSc Thesis. University of Houston, 103 pp.

577 IGME, 1990a. Documentos sobre la geología del subsuelo de España: Cantábrica.
578 Instituto Geológico y Minero de España, VII, Madrid, 45 pp.

579 IGME, 1990b. Documentos sobre la geología del subsuelo de España: Ebro-Pirineos.
580 Instituto Geológico y Minero de España, VI, Madrid, 87 pp.

581 Jackson, M.P.A., Seni, S.J., 1983. Geometry and evolution of salt structures in a
582 marginal rift basin of the Gulf of Mexico, East Texas. Geology, 11, 131–135.

583 Koyi, H., 2001. Modeling the influence of sinking anhydrite blocks on salt diapirs
584 targeted for hazardous waste disposal. Geology 29, 387–390.

585 Lehné R.J., Sirocko, F., 2010. Recent vertical crustal movements and resulting surface
586 deformation within the North German Basin (Schleswig-Holstein) derived by GIS-
587 based analysis of repeated precise leveling data. Zeitschrift der Deutschen Gesellschaft
588 für Geowissenschaften 161, 175–188.

589 Larsen, G, Chilingar, G.V., 1983. Diagenesis in sediments and sedimentary rocks.
590 Elsevier, Amsterdam, 572 pp.

591 Looff, K.M, Looff, K.M., Rautman, C., 2010. Salt spines, boundary shear zones and
592 anomalous salts: Their characteristics, detection and influence on salt dome storage
593 caverns. Solution Mining Research Institute Spring, Technical Conference Grand
594 Junction, Colorado, USA, pp. 26-27.

595 Lucha, P., Cardona, F., Gutiérrez, F, Guerrero, J., 2008. Natural and human-induced
596 dissolution and subsidence processes in the salt outcrop of the Cardona Diapir (NE
597 Spain). Environmental Geology 53, 1023–1035.

598 Mackay, J.R., 1998. Pingo growth and collapse, Tuktoyaktuk Peninsula Area, western
599 Arctic Coast, Canada: a long-term field study. Géographie Physique et Quaternaire 52,
600 271–323.

601 McCalpin, J.P., 2009. Paleoseismology in extensional tectonic environments. In:
602 McCalpin, J.P. (Ed.), Paleoseismology. Academic Press, San Diego, California, pp.
603 171–-277.

604 McCalpin, J.P., Hart, E.W., 2002. Ridge-top spreading features and relationship to
605 earthquakes, San Gabriel Mountain region, southern California. Contributions 3 and 4.
606 In: Hart, E.W. (Ed.), Ridge-top spreading in California, contributions towards
607 understanding a significant seismic hazard. California Geological Survey, CD 2003-05,
608 disk 1 of 2.

609 Muñoz, J.A., 1992. Evolution of a continental collision belt: ECORS-Pyrenees crustal
610 balanced cross-section. In: McKlay, K.R. (Ed.), Thrust tectonics. Chapman and Hall,
611 New York, pp. 235–246.

612 Nocquet, J.M., 2012. Present-day kinematics of the Mediterranean: a comprehensive
613 overview of GPS results. Tectonophysics 579, 220–242.

614 Olive, A., López-Horgue, M.A., Baceta, J., Niñero, S., Villanueva, E., 2010. Memoria y
615 mapa geológico de Navarra de la hoja de Lezaun (140) a escala 1:25.000. Gobierno de
616 Navarra, Departamento de obras públicas, transportes y comunicaciones, Pamplona.

617 Parkhurst, D.L., Appelo, C.A.J., 2013. Description of input and examples for
618 PHREEQC version 3-A computer program for speciation, batch-reaction, one-
619 dimensional transport, and inverse geochemical calculations. U.S. Geological Survey
620 Techniques and Methods 6, A43, 497pp. Available only at
621 http://pubs.usgs.gov/tm/06/a43/

622 Payros, A., 1997. El Eoceno de la Cuenca de Pamplona: Estratigrafia secuencial y
623 evolución paleogeográfica. PhD Thesis. Basque Country University, Bilbao.

624 Payros, A., Pujalte, V., Baceta, J.I., Orue-Etxebarria, X., Serrakiel, J., 1996. Las calizas
625 eocenas del Oeste de Navarra: revisión, redefinición y nueva interpretación de sus
626 unidades estratigráficas. In: Astibia, H., Valle, J., Murelaga, X., Serrakiel, J. (Eds.),
627 Libro Homenaje a Máximo Ruiz de Gaona, Príncipe de Viana, Gobierno de Navarra,
628 Pamplona, pp. 137–153.

629 Pinto, V., Casas, A., Rivero, L., Torné, M., 2005. 3D gravity modeling of the Triassic
630 salt diapirs of the Cubeta Alavesa (northern Spain). Tectonophysics 405, 65–75.

631 Poprawski, Y., Basile, C., Agirrezabala, L.M., Jaillard, E., Gaudin, M. Jacquin, T.,
632 2014. Sedimentary and structural record of the Albian growth of the Bakio salt diapir
633 (the Basque Country, northern Spain). Basin Research 26, 746–766.

634 Quintà, A., Tavani, S., Roca, E., 2012. Fracture pattern analysis as a tool for
635 constraining the interaction between regional and diapir-related stress fields: Poza de la
636 Sal Diapir (Basque Pyrenees, Spain). In: Alsop, G.I., Archer, S.G., Hartley, A.J., Grant,
637 N.T., Hodgkinson, R. (Eds.), Salt Tectonics, sediments and prospectivity. Geological
638 Society, London, Special Publications 363, 521–532.

639 Ramírez, J.I., Olive, A., Alvaro, M., Ramírez del Pozo, J., Meléndez, A., Gutiérrez
640 Elorza, M., Carbayo, A., Villalobos, L., León, L., Gabaldón, V., 1987. Mapa Geológico
641 de España 1:50.000 Estella, Hoja 140. 1ª Edición. Instituto Geologico y Minero de
642 España, Gráficas Topacio, Madrid.

643 Salvany, J.M., 1990. Introducción a las evaporitas triásicas de las cadenas periféricas de
644 la cuenca del Ebro: Catalánides, Pirineo y Región Cantábrica. In: Orti, F., Salvany, J.
645 M. (Eds.), Formaciones evaporíticas de la Cuenca del Ebro y cadenas periféricas y de la
646 zona de Levante. ENRESA-GPPG, Universidad de Barcelona, pp. 9–20.

647 Santolaria, P., Vendeville, B.C., Graveleau, F., Soto, R., Casas-Sainz, A., 2015. Double
648 evaporitic décollements: Influences of pinch-out overlapping in experimental thrust
649 wedges. Journal of Structural Geology 76, 35–51.

650 Sans, M., 2003. From thrust tectonics to diapirism. The role of evaporites in the
651 kinematic evolution of the eastern South Pyrenean front. Geol Acta 1, 239–259.

652 Sans, M., Verges, J., 1995. Fold development related to contractional salt tectonics:
653 Southeastern Pyrenean Thrust Front, Spain. In: Jackson, M.P.A., Roberts, D.G.,
654 Snelson, S. (Eds.), Salt tectonics: a global perspective. AAPG Memoir 65, pp. 369–378.

655 Serrano, A., Martinez del Olmo, W. 1990. Tectónica salina en el Dominio Cántabro–
656 Navarro: evolución, edad y origen de las estructuras salinas. In: Orti, F., Salvany, J.M.
657 (Eds.), Formaciones evaporíticas de la Cuenca del Ebro y cadenas periféricas y de la
658 zona de Levante: Nuevas Aportaciones y Guía de Superficie. Empresa Nacional De
659 Residuos Radiactivos S.A, ENRESA-GPPG, Barcelona, pp. 39–53.

660 Serrano, A., Martínez del Olmo, W., 2004. Estructuras diapíricas de la zona meridional
661 de la Cuenca Vasco-Cantábrica. In: Vera, J.A. (Ed.), Geología de España. Sociedad
662 Geológica de España, Instituto Geológico y Minero de España, Madrid, pp. 334–338.

663 Smith, R.I., Hodgson, N., Fulton, M.M., 1993. Salt control on Triassic reservoir
664 distribution, UKCS Central North Sea. In: Parker, J.R. (Ed.), Petroleum Geology of
665 Northwest Europe: Proceedings of the 4th Conference. Geological Society, London, pp.
666 547–557.

667 Stewart, S.A., 2006. Implications of passive salt diapir kinematics for reservoir
668 segmentation by radial and concentric faults. Marine and Petroleum Geology 23, 843–
669 853.

670 Stewart, S.A., Clarke, J.A., 1999. Impact of salt on the structure of the Central North
671 Sea hydrocarbon fairways. Petroleum Geology Conference Series 5, 179–200.

672 Stuiver, M., Reimer, P.J., Reimer, R.W., 2019. CALIB 7.1 program. At http://calib.org.

673 Vendeville, B.C., Jackson, M.P.A., 1992. The rise of diapirs during thin-skinned
674 extension. Marine and Petroleum Geology, 9, 331–353.

675 Vendeville, B.C, Nilsen, K.T., 1995. Episodic growth of salt diapirs driven by
676 horizontal shortening. GCSSEPM Foundation, 16th Annual Research Conference Salt,
677 Sediment and Hydrocarbons, 285–295.

678 Vergés, J., Fernàndez, M., Martínez, A., 2002. The Pyrenean orogen: pre-, syn-, and
679 post-collisional evolution. In: Rosenbaum, G., Lister, G.S. (Ed.), Reconstruction of the
680 evolution of the Alpine-Himalayan Orogen. Journal of the Virtual Explorer 8, pp. 55–
681 74.

682 Walter, T.R., Troll, R., 2001. Formation of caldera periphery faults: an experimental
683 study. Bulletin of Volcanology 63, 191–203.

684 Weinberger, R., Begin, Z.B., Waldmann, N., Gardosh, M., Baer, G., Frumkin, A.,
685 Wdowinski, S., 2006. Quaternary rise of the Sedom diapir, Dead Sea Basin. In: Enzel,
686 Y., Agnon, A., Stein, M. (Eds.), New Frontiers in Dead Sea. Paleoenvironmental
687 Research. Geological Society of America Special Paper 401, pp. 33–51.

688 Wetzler, N., Sagy, A., Marco, S., 2011. Seismological observations of micro-earthquake
689 clusters, Dead Sea basin. American Geophysical Union Fall Meeting, American
690 Geophysical Union. Washington. Abstract #S21A–2160.

691 Wierzbicki, R., Dravis, J.J., Al-Aasm, I., Harland N., 2006. Burial dolomitization and
692 dissolution of Upper Jurassic Abenaki platform carbonates, Deep Panuke reservoir,
693 Nova Scotia, Canada. AAPG Bulletin 90, 1843–1861.

694 Yamada, Y., Okamura, H., Tamura, Y., Tsuneyama, F., 2005. Analog models of faults
695 associated with salt doming and wrenching: application to offshore United Arab
696 Emirates. In: Sorkhabi, R., Tsuji, Y. (Eds.), Faults, Fluid Flow, and Petroleum Traps.
697 American Association of Petroleum Geologists (AAPG) Memoir 85. AAPG, Tulsa, OK,
698 pp. 95–106.

699 Yu, J., Wang, G., 2016. GPS-derived ground deformation (2005–2014) within the Gulf
700 of Mexico region referred to a stable Gulf of Mexico reference frame. Natural Hazards
701 and Earth System Sciences 16, 1583–1602.

Zarei M., Raeisi E., 2010. Karst development and hydrogeology of Konarsiah salt diapir, south of Iran. Carbonates and Evaporites 25, 217–229.

Zarei M., 2016. Factors governing the impact of emerged salt diapirs on water resources. Groundwater 54, 354–362.

Zirngast, M., 1996. The development of the Gorbelen salt dome (NW Germany) based on quantitative analysis of peripheral sinks. In: Alsop, G.I., Blundell D.J., Davison, I. (Eds.), Salt tectonics. Geological Society, London, Special Publication 100, pp. 203-226.

Figure Captions

Figure 1. Geological and geomorphological map of the Salinas de Oro diapir showing the cross-cutting relationship between radial grabens and concentric faults and the location of saline springs and sampling stations.

Figure 2. A) Radial grabens crosscutting the Mesozoic and Tertiary overburden at the diapir edge. B) Radial graben overlapping concentric faults developed on the limestone rim. C) Panoramic view of Azanza Graben and location of the trench. D) Active ring faults and elongated sinkhole at the eastern diapir edge at the contact with the limestone overburden. E and F) S1-S2 high-concentration springs at the bottom of the valley.

Figure 3. Correlation between hydrochemical parameters in the water samples. A) Sodium vs. Chloride dissolved concentrations; B) Calcium and magnesium vs. sulfate dissolved concentrations; C) Magnesium vs. calcium dissolved concentrations, with indication of the S1 spring water.

Figure 4. Shaded relief map and geomorphology of Azanza graben showing the location of the trench close to the tip of the western radial fault.

Figure 5. Log of the W wall of the trench. Indicated error range of C14 samples is at 2 sigma. See location in Figs. 2C and 4 and explanation in text. The photographs illustrate the geomorphic setting of the trench excavated across the western radial fault scarp (A), faults truncated by the overlying sediments and soil (B and C) and the tilting of the graben fill and weathered bedrock (D).

Table 1 and 2

Sampling points	Date	Cond	TDS	pH	HCO_3^-	Cl^-	SO_4^{2-}	Ca^{2+}	Mg^{2+}	Na^+	K^+	Ionic Balance
A	20/05/2017	3.9	3749	8.2	277	1870	177	155	27	1226	17	1.66
	10/09/2018	4.4	3954	8.25	281	1950	202	158	28	1316	19	2.51
S1	20/05/2017	160.1	114287	7.01	232	64300	4545	1120	280	42900	910	0.82
	10/09/2018	>200	137077	7.07	245	75100	5542	1200	310	53800	880	3.87
S2	20/05/2017	104.3	79780	7.82	170	45600	3067	1060	170	29340	373	-0.63
	10/09/2018	121.2	91125	7.49	272	50500	4676	1700	240	33700	37	0.85
S3	20/05/2017	117.6	88664	7.59	253	49400	4193	1530	184	32590	514	0.63
	10/09/2018	165.4	91102	7.55	272	50900	4765	1520	202	33400	43	-0.39
S4	20/05/2017	24.4	15529	7.84	85	7320	2247	850	117	4880	30	1,50
S5	20/05/2017	30.2	18900	8.43	220	10500	880	280	51	6940	29	-0.20
B	20/05/2017	85.5	61276	8.17	240	35100	2352	860	135	22350	239	-1.14
	10/09/2018	97.3	70732	8.2	206	40500	2695	970	152	25830	379	-0.95

Table 1. Major ion concentrations and TDS (total dissolved solids) in mg/l and conductivity in mS/cm of the brine springs (S1 to S4) and the sampling stations A and B located before and after the emergence of the saline springs.

Date	Cond	TDS	T^a	pH	HCO_3^-	Cl^-	SO_4^{2-}	Ca^{2+}	Mg^{2+}	Na^+	K^+
01/03/2007	78600	62299.9	16.1	8.4	149	35900	2480	501	69	23200	293
03/07/2007	50000	40649.6	21.9	8.6	203	24100	1533	572	90	14150	179
04/10/2007	52300	29708.9	17.2	8.3	169	12210	1584	590	86	15070	125
17/01/2008	38100	26140.5	6.4	8.4	231	15415	1188	384	52	8870	108
03/04/2008	27600	18747.1	12.8	8	325	10430	832	358	42	6760	74
03/07/2008	37600	26202.7	19.8	8.5	244	15050	1004	438	66	9400	108
02/10/2008	80600	59249	15	8.2	147	32650	1748	950	154	23600	276
15/01/2009	46400	33427.5	2.6	8.3	264	18995	1252	501	75	12340	143
01/04/2009	44200	30778	8.6	8.5	210	17460	1193	478	77	11360	130
02/07/2009	74900	58159	24.8	8.3	136	32110	2150	879	144	22740	270
28/10/2010	>45000	66000	14.1	8.4	110	37800	2570	892	148	24480	313
23/03/2011	35000	24577	15.4	8.7	214	13900	1010	403	50	9000	100
09/05/2011	61900	47140	28,6	8,6	87	26900	1930	684	109	17430	212
22/06/2011	91600	67319,5	24,1	8,4	133	37060	2637	701	88,5	26700	320
14/12/2011	89100	66170	8	8,3	156	37900	2630	826	158	24500	314
09/05/2012	24100	17238,5	25,6	8,5	207	9250	813	322	46	6600	67
12/07/2012	89400	79659	25,6	8,5	94	45590	3310	1020	165	29480	388
18/10/2012	104500	84983	15	8,3	104	48600	3280	1160	209	31630	418
24/01/2013	2460	1457,8	5,6	8,4	145	656	139	92,1	8,7	417	4
03/12/2013	52300	35061	5,8	8,4	160	19700	1480	495	76	13150	151

Table 2. Major ionic concentration and TDS in (mg/l) and conductivity in mS/cm of the Salado Creek at Estenoz Gauging Station located 2 km downstream Salinas de Oro Diapir from 2007 to 2013 obtained from the CHE database. Dissolved K concentrations were not available for some of the samples and they have been estimated from other samples with similar TDS contents.

Figure 1

Click here to download high resolution image

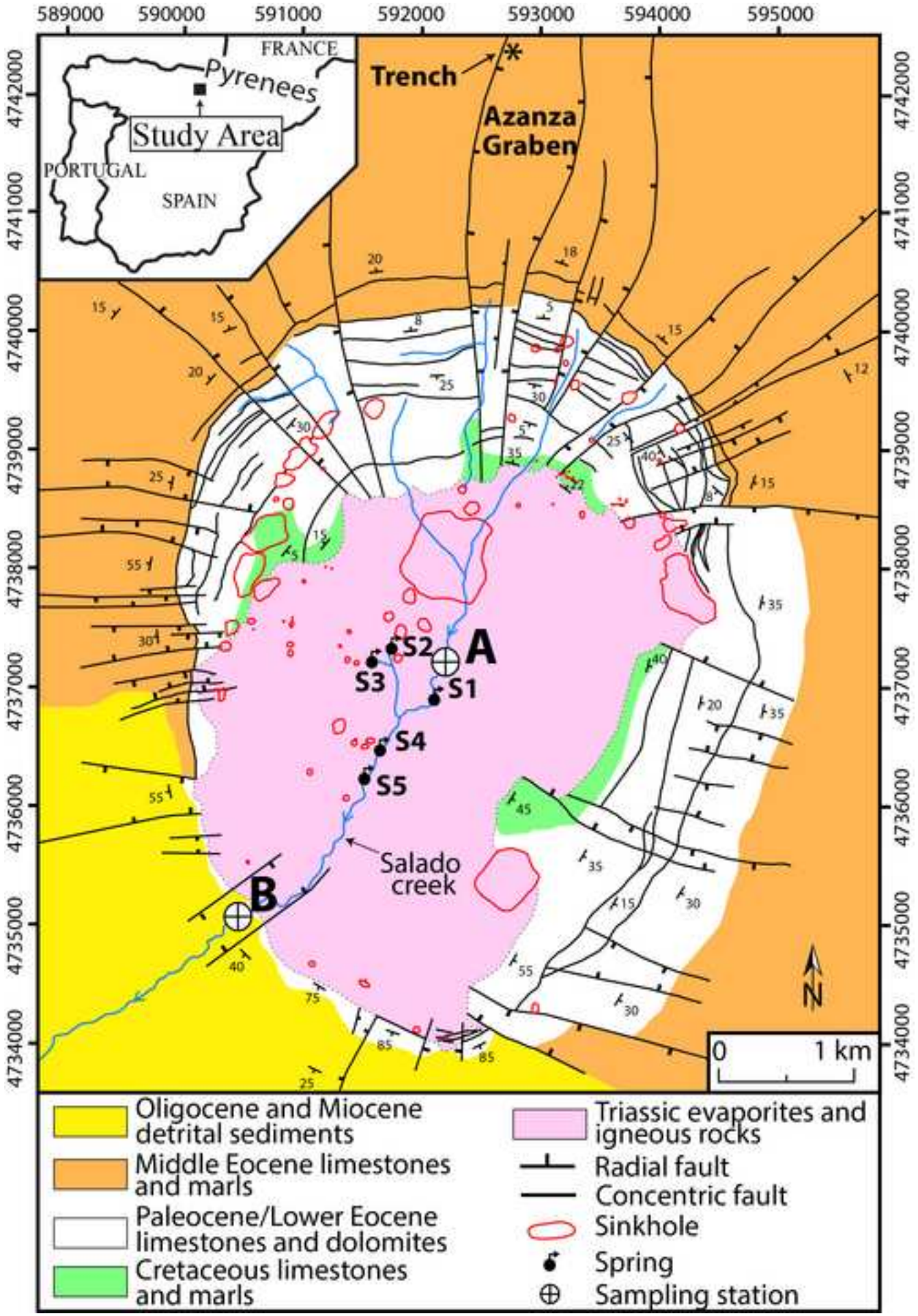

Figure 2

Click here to download high resolution image

Figure 3

Click here to download high resolution image

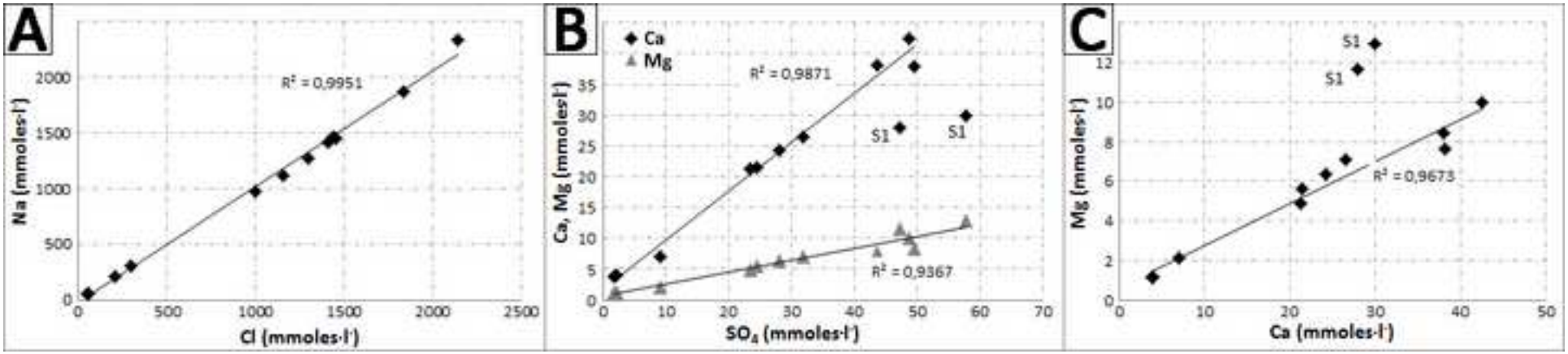

Figure 4

Click here to download high resolution image

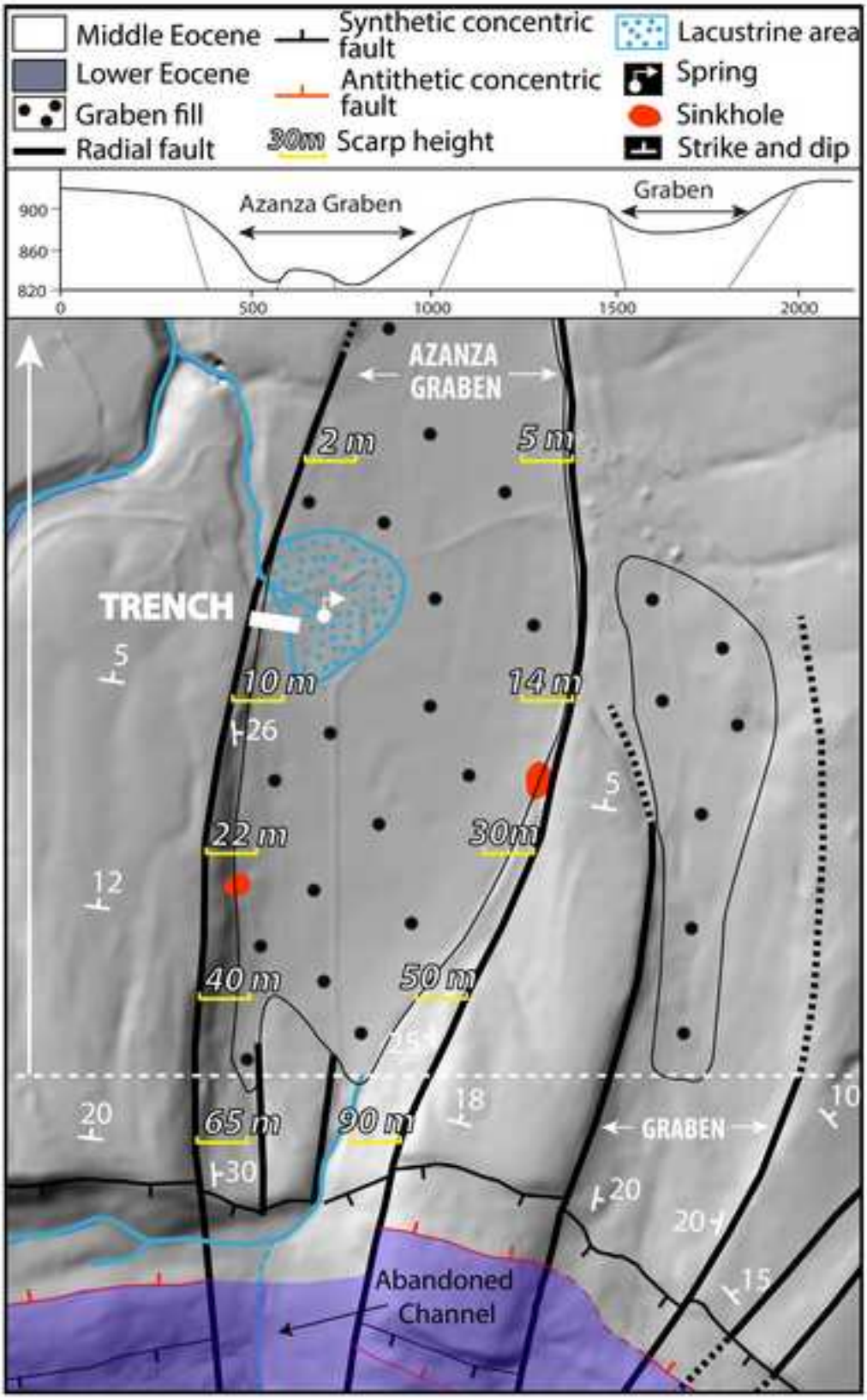

Figure 5

Click here to download high resolution image

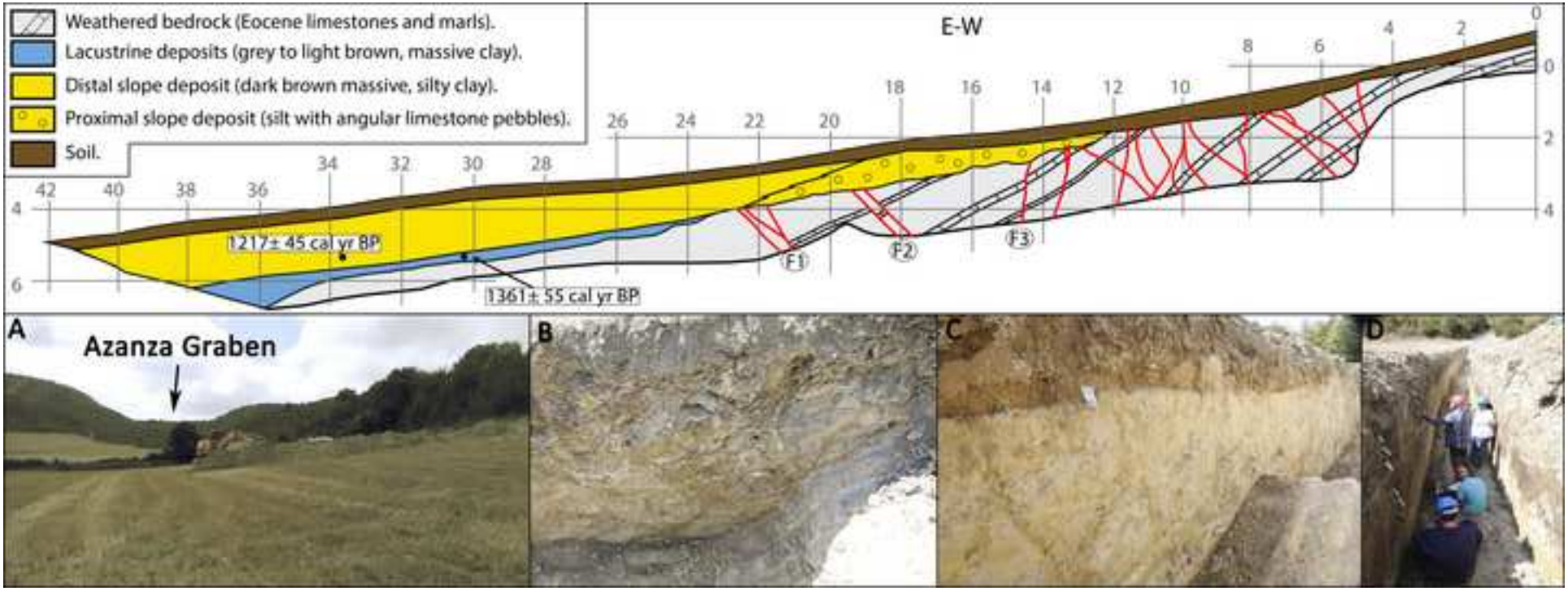

Figure 1 (Greyscale)

Click here to download high resolution image

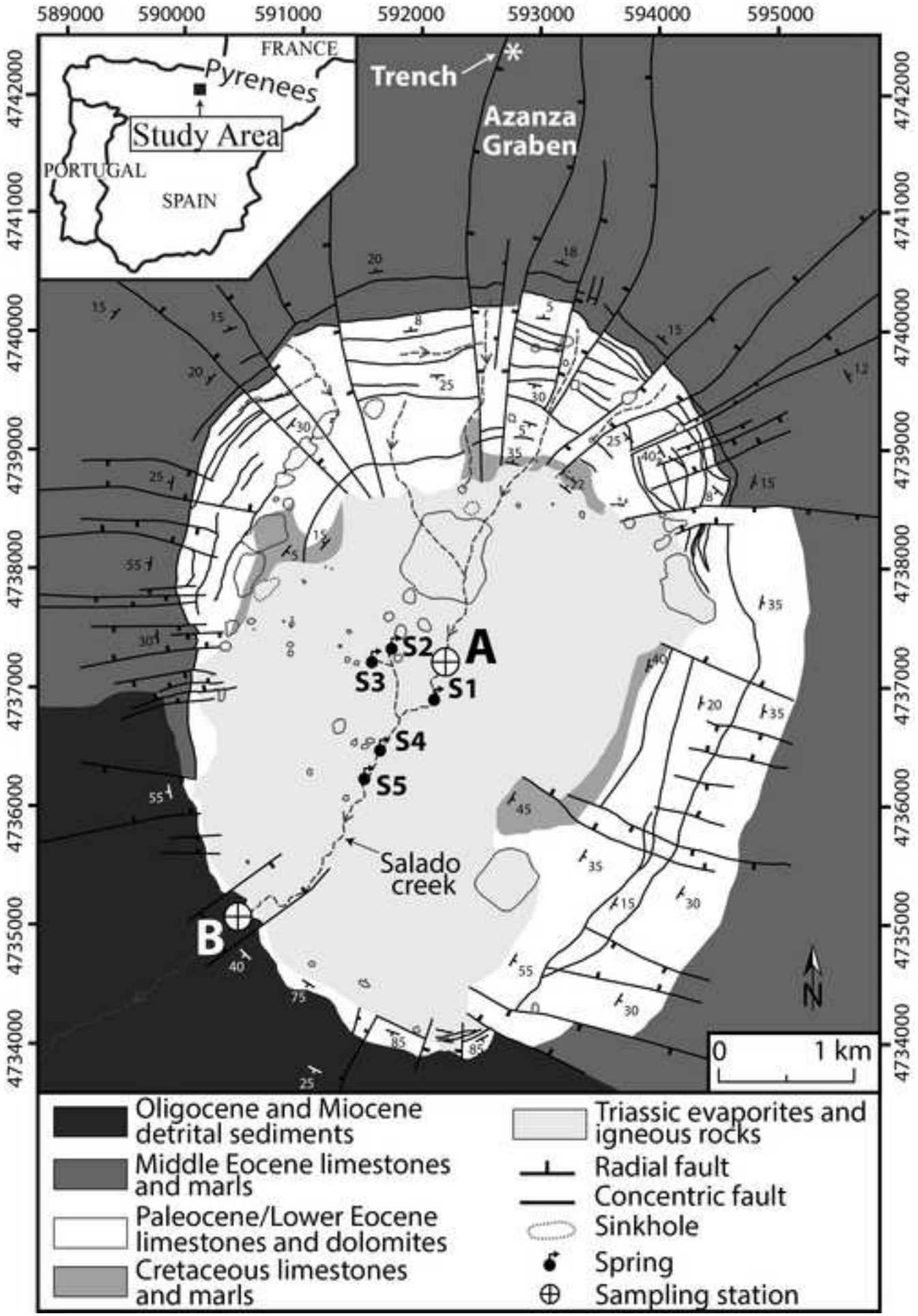

Figure 2 (Greyscale)
Click here to download high resolution image

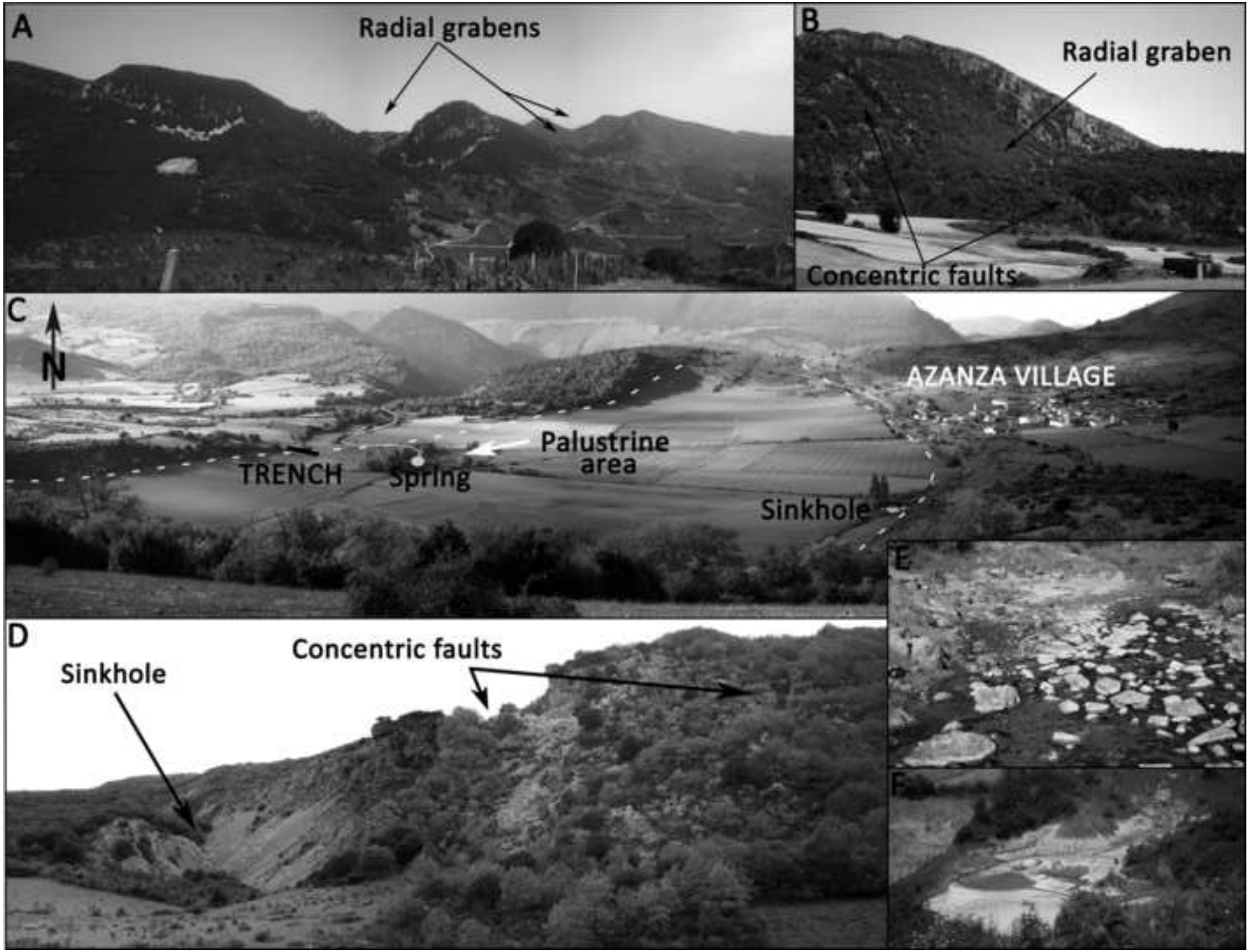

Figure 4 (Greyscale)
Click here to download high resolution image

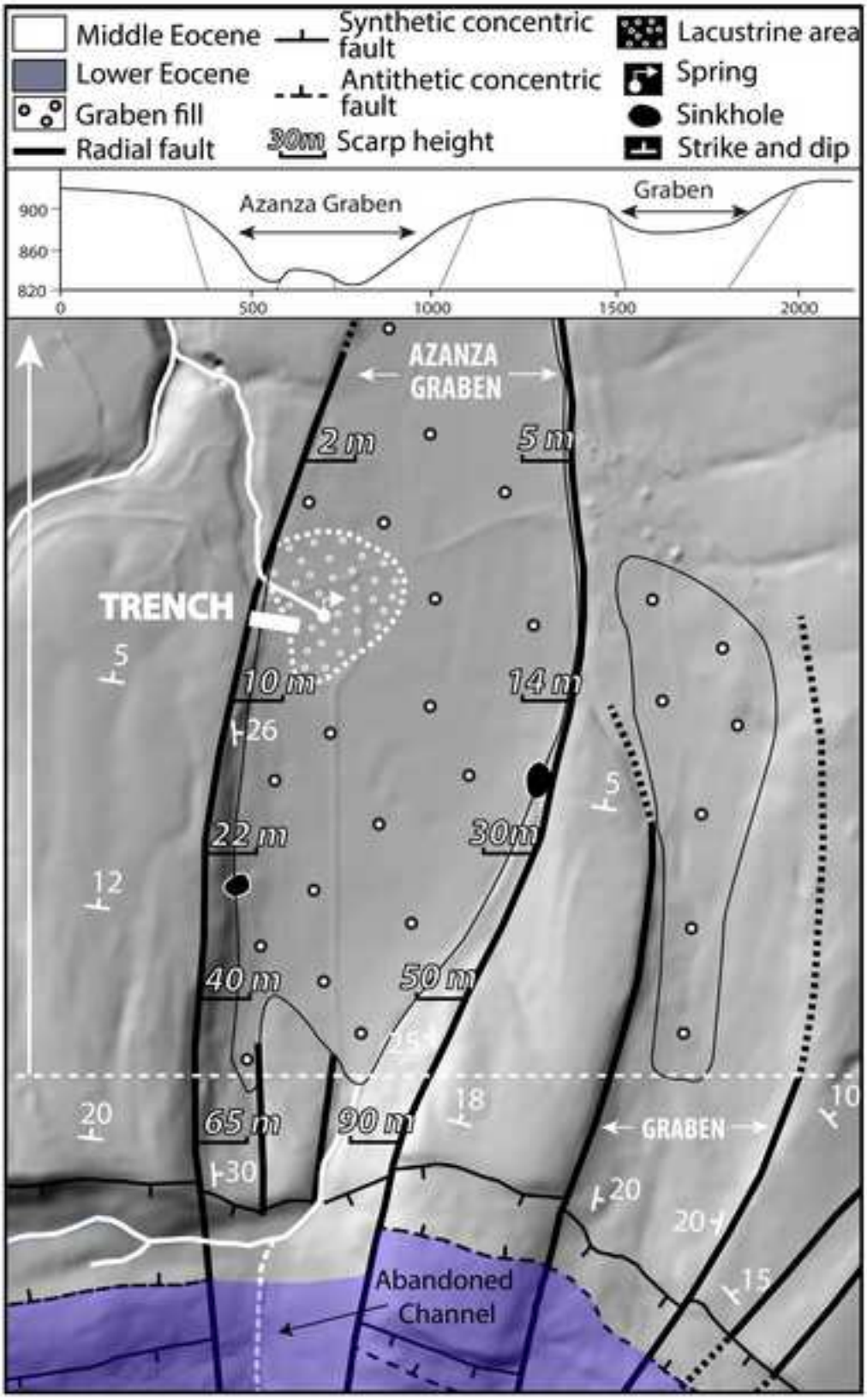

Figure 5 (Greyscale)
Click here to download high resolution image